

Handover-Aware Power Minimization for Networked LEO Satellite Communications: Joint Cooperative Beamforming and Scheduling

Yuchen Zhang, *Member, IEEE*, Eva Lagunas, *Senior Member, IEEE*,
Symeon Chatzinotas, *Fellow, IEEE*, and Tareq Y. Al-Naffouri, *Fellow, IEEE*

Abstract—Networked low Earth orbit (LEO) satellite constellations enabled by inter-satellite links offer a promising path toward ubiquitous broadband non-terrestrial services. However, fast orbital motion induces frequent scheduling updates and handovers, while stringent on-board constraints (e.g., limited radio-frequency chains) tightly couple user scheduling with cooperative beamforming. This paper investigates *handover-aware* power-efficient downlink transmission in networked LEO systems under statistical channel state information. We introduce a two-segment frame structure that separates handover-related operations from user-plane transmission, and propose a power consumption model that captures both the switching cost of newly established satellite-user links and the reduced effective transmission window during handover. Using a hardening-bound ergodic-rate metric, we formulate a per-frame network-wide power minimization problem with joint cooperative beamforming and implicit scheduling under segmented quality-of-service constraints, per-satellite power budgets, and serving-cardinality limits. To address scheduling-induced combinatorial sparsity and nonconvex fractional rate constraints, we develop an iterative algorithm that combines a reweighted ℓ_2 surrogate with a penalty-based relaxation and a fractional-programming inner loop, yielding a sequence of convex second-order cone programs. Simulations based on time-varying orbital dynamics with frame-wise serving-set evolution and maritime user data quantify the power-handover tradeoff and demonstrate consistent power savings and improved feasibility over non-cooperative and pre-scheduled cooperative baselines.

Index Terms—LEO satellite communication, handover, cooperative beamforming, user scheduling.

I. INTRODUCTION

Non-terrestrial networks (NTNs) are increasingly recognized as a key component of the sixth generation (6G) ecosystem for enabling ubiquitous *broadband* connectivity and bridging the digital divide, especially over sparsely populated and hard-to-reach areas [1]–[5]. Among various NTN platforms, low Earth orbit (LEO) satellite constellations have attracted substantial attention from both academia and industry

due to their lower orbital altitudes, which translate into reduced propagation latency and stronger received signal strength compared with medium Earth orbit (MEO)/geostationary Earth orbit (GEO) systems [3], [6]. In addition, the adoption of regenerative payloads and large antenna arrays on-board LEO satellites further strengthens their potential to support high-throughput services [7]–[9].

Despite these advantages, achieving terrestrial-network-like service quality over LEO systems remains challenging due to factors such as the long propagation distance and stringent on-board power constraints. This motivates a paradigm shift from conventional *single-satellite* service to *multi-satellite cooperation*. With the maturation of inter-satellite links (ISLs) technologies [10], multiple LEO satellites can be interconnected to enable *networked LEO cooperation*, where several satellites jointly serve users via cooperative beamforming [11]–[18]. This cooperation can be viewed as a non-terrestrial counterpart of terrestrial cell-free massive multi-input-multi-output (MIMO), coordinating distributed transmitters to exploit additional spatial degree of freedom (DoF) for interference mitigation and link-budget enhancement [19]–[22].

There has been a growing body of work on networked LEO cooperative transmission, addressing cooperative beamforming, resource allocation, and statistical-channel state information (CSI)-based designs under LEO-specific channel characteristics [11], [12], [17], [18], [21]. However, most existing formulations are rate-centric (e.g., sum-rate or min-rate maximization), while a more practically relevant question in LEO systems is *how to minimize power consumption subject to prescribed service rates*. This is because LEO satellites operate under stringent on-board energy and payload constraints (e.g., limited power generation, battery capacity, and thermal budgets), making energy-efficient operation a first-order design goal [4], [5], [9]. Moreover, due to limited on-board resources such as the number of radio frequency chains (RFCs), each satellite can serve only a small subset of user terminals (UTs) simultaneously, which necessitates *user scheduling*. Yet, in many existing works, scheduling is either ignored or handled in a decoupled manner, e.g., by prefixing scheduling and then optimizing beamforming [11], [18], which can incur notable performance loss because scheduling and cooperative beamforming are intrinsically coupled through multi-user interference and cooperation patterns.

While networked LEO cooperation offers significant perfor-

This publication is based upon work supported by King Abdullah University of Science and Technology (KAUST) under Award No. ORFS-CRG12-2024-6478 and Global Fellowship Program under Award No. RFS-2025-6844.

Yuchen Zhang and Tareq Y. Al-Naffouri are with the Electrical and Computer Engineering Program, Computer, Electrical and Mathematical Sciences and Engineering (CEMSE), King Abdullah University of Science and Technology (KAUST), Thuwal 23955-6900, Kingdom of Saudi Arabia (e-mail: {yuchen.zhang; tareq.alnaffouri}@kaust.edu.sa).

Eva Lagunas and Symeon Chatzinotas are with the Interdisciplinary Centre for Security, Reliability and Trust (SnT), University of Luxembourg, 1855 Luxembourg City, Luxembourg (e-mail: {eva.lagunas; Symeon.Chatzinotas}@uni.lu).

mance gains, LEO orbital dynamics introduces an additional challenge that is far less pronounced in terrestrial systems. In particular, LEO satellites traverse at orbital velocities of several kilometers per second, leading to rapid changes in geometry and link visibility. As a result, the satellite-UT serving pattern must be updated frequently, triggering *handover* procedures that incur signaling overhead, consume dedicated radio resources, and may interrupt user-plane transmission [4], [23]. This issue becomes even more intricate in networked LEO cooperation: the many-to-many service paradigm implies that a scheduling update may activate/deactivate multiple satellite-UT links, thereby amplifying switching overhead and potentially inducing substantial *handover-related power cost*. Without explicitly accounting for this effect, system evaluation can be overly optimistic and the resulting design may become short-sighted, incurring excessive switching under dynamic topology.

The handover issue in NTN has been investigated from multiple angles, ranging from protocol support and signaling procedures in 3rd generation partnership project (3GPP) new radio (NR)-NTN to mobility management under time-varying satellite visibility [4], [5]. Recent LEO-focused studies have improved mobility robustness by redesigning handover procedures to cope with long propagation delays (e.g., predictive/learning-based protocols) [24], refining handover triggering and access selection using geometry- or gain-aware criteria [23], [25], and mitigating handover-induced performance loss through transmission/beamforming adaptations or multi-orbit joint service mechanisms [26], [27]. While these works are instrumental for reducing access delay, failures, and service interruption, they typically treat handover as a mobility-protocol or link-reliability problem and do not provide an explicit *handover-induced power/switching-cost* modeling layer that can be embedded into *networked* multi-satellite cooperation with limited on-board resources. Consequently, *how to minimize handover-aware network-wide power consumption via joint networked LEO cooperative beamforming and user scheduling* remains largely open.

Motivated by the above gaps, this paper develops a handover-aware power minimization framework for networked LEO satellite downlinks with joint cooperative beamforming and user scheduling. In addition, obtaining accurate instantaneous CSI can be challenging in LEO systems due to fast channel variation and non-negligible round-trip latency, which motivates performance evaluation and optimization based on statistical-CSI metrics [11], [21]. Accordingly, we adopt the hardening bound as a tractable lower bound on the ergodic downlink rate, enabling per-UT quality of service (QoS) constraints that depend only on statistical channel parameters [28], [29]. The main contributions are summarized as follows:

- **Handover-aware power consumption modeling:** We introduce a two-segment frame structure that separates handover-related operations from user-plane data transmission, and propose a handover-aware power consumption model that explicitly captures (i) per-link handover-related power cost when establishing new satellite-UT connections and (ii) the reduced effective transmis-

sion window induced by handover, thereby coupling consecutive-frame scheduling decisions with network-wide power expenditure.

- **Handover-aware joint power minimization and algorithmic solution:** Under the proposed modeling layer and statistical-CSI hardening-bound rate metric, we formulate a per-frame network-wide power minimization problem that jointly optimizes cooperative beamforming and implicit LEO-UT scheduling subject to segmented QoS constraints, per-satellite radiated power budgets, and per-satellite serving-cardinality constraints. The resulting problem is challenging due to scheduling-induced combinatorial sparsity and the nonconvex fractional structure of the segmented statistical-rate constraints. To obtain a tractable design, we develop an iterative algorithm that (i) promotes per-satellite stream sparsity via a reweighted ℓ_2 surrogate with a penalty-based relaxation for robustness, and (ii) handles the segmented QoS constraints using a fractional programming (FP)-based inner loop, leading to a sequence of convex second-order cone programmings (SOCPs) solvable by standard tools.
- **Systematic evaluation with orbital dynamics and real user data:** We conduct extensive Monte-Carlo simulations under time-varying LEO orbital dynamics with frame-wise serving-set evolution, using a Walker-Delta constellation and maritime user locations. The results quantify the power-handover tradeoff and show that the proposed handover-aware joint design consistently reduces network-wide power and improves feasibility over time compared with non-cooperative baselines and cooperative schemes with pre-fixed scheduling.

The remainder of this paper is organized as follows. Section II presents the system and channel models. Section III introduces the frame structure and handover-aware power and statistical-rate metrics. Section IV formulates the handover-aware joint optimization problem and develops the proposed iterative algorithm. Section V provides numerical results under dynamic topology. Finally, Section VI concludes the paper.

Notations: Scalars are denoted by lowercase letters, while vectors and matrices are denoted by bold lowercase and bold uppercase letters, respectively. The Euclidean norm of a vector \mathbf{a} is written as $\|\mathbf{a}\|$. The transpose and Hermitian transpose are denoted by $(\cdot)^T$ and $(\cdot)^H$, respectively. For a matrix \mathbf{A} , $\text{Tr}(\mathbf{A})$ denotes the trace, and $\text{diag}(\mathbf{a})$ denotes the diagonal matrix with diagonal entries given by \mathbf{a} . The real and imaginary parts of a complex scalar a are denoted by $\Re\{a\}$ and $\Im\{a\}$, respectively. The block-diagonal matrix with blocks $\mathbf{A}_1, \dots, \mathbf{A}_N$ is denoted by $\text{blkdiag}(\mathbf{A}_1, \dots, \mathbf{A}_N)$. The Kronecker product is denoted by \otimes . The indicator function is denoted by $1_{\{x\}}$, which equals 1 if $x > 0$ and 0 otherwise. Finally, $\mathcal{CN}(\mathbf{a}, \mathbf{C})$ denotes a circularly symmetric complex Gaussian distribution with mean \mathbf{a} and covariance matrix \mathbf{C} .

II. SIGNAL AND CHANNEL MODELS

As illustrated in Fig. 1, we consider cooperative downlink communications in a *networked* LEO satellite system. A set

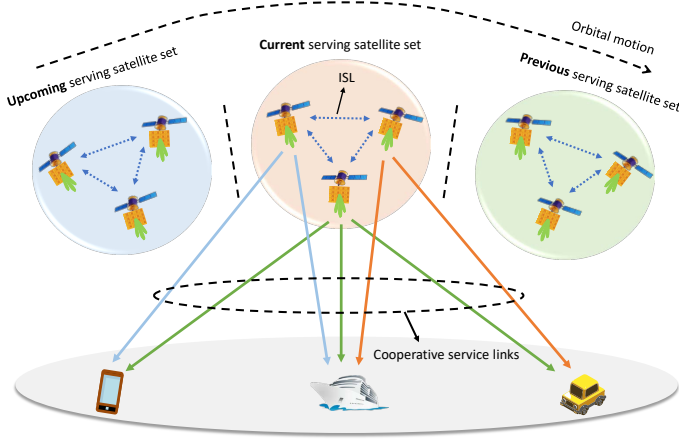


Fig. 1. Illustration of system model. The cooperating LEO satellites are typically separated by hundreds to a few thousand kilometers, depending on the orbital configuration and the selected serving set.

of L regenerative LEO satellites jointly serves a group of U UTs, each modeled as a single-antenna receiver with an omnidirectional (or quasi-omnidirectional) terminal pattern. This abstraction is suitable for handheld-user access and for user terminals embedded in application scenarios such as vehicles or vessels, while the icons in Fig. 1 are intended only to illustrate representative service environments rather than to specify the terminal antenna hardware. Each satellite employs a half-wavelength-spaced uniform planar array (UPA) comprising $N = N_h \times N_v$ antenna elements, where N_h and N_v denote the numbers of antennas along the horizontal and vertical dimensions, respectively. The L satellites are interconnected via ISLs, enabling cooperative transmission. We assume that the ISL connectivity supports exchange of the coordination information required by the proposed design (e.g., via a connected backbone), without committing to a particular routing/topology. The L satellites closest to the geographical center of the UTs are selected from the entire LEO constellation, which is motivated by the LEO channel being predominantly line-of-sight (LoS) and geometry-driven [7], [11], [18], so satellites with smaller slant ranges to the service region typically provide stronger links. Nevertheless, other selection criteria can also be incorporated.

Due to the high orbital velocity of LEO satellites (e.g., approximately 7.6 km/s at an orbital altitude of 500 km), the L -satellite serving set varies over time. In contrast, the membership of the UT set typically evolves on a much slower timescale and is therefore assumed to remain fixed. To account for orbital dynamics in a tractable manner, we adopt a frame-wise model consisting of K frames. It is assumed that no satellite membership change occurs within a single frame, while the serving satellite set is re-evaluated at the beginning of each new frame. Specifically, in the k -th frame, the index set of the selected L satellites is denoted by $\mathcal{L}^{(k)}$.

A. Downlink Signal Model

In the k -th frame, the satellites in $\mathcal{L}^{(k)}$ cooperatively transmit U independent data streams. We assume that the satellites in $\mathcal{L}^{(k)}$ are synchronized in time/frequency/phase and have

access to all user data streams (e.g., via feeder links and/or ISLs) to support coherent joint transmission [11], [12], [21]. The transmit signal of the ℓ -th satellite is expressed as

$$\mathbf{x}_\ell^{(k)} = \sum_{u=1}^U \mathbf{w}_{\ell,u}^{(k)} s_u^{(k)} = \mathbf{W}_\ell^{(k)} \mathbf{s}^{(k)}, \quad (1)$$

where $\mathbf{W}_\ell^{(k)} = [\mathbf{w}_{\ell,1}^{(k)}, \dots, \mathbf{w}_{\ell,U}^{(k)}] \in \mathbb{C}^{N \times U}$ stacks the beamforming vectors from the ℓ -th satellite to all UTs. Owing to the limited number of RFCs available at each satellite, which is typically smaller than U , user scheduling naturally arises. Specifically, each satellite can simultaneously serve at most U_{\max} UTs, implying that only U_{\max} columns of $\mathbf{W}_\ell^{(k)}$ can be nonzero, while the remaining beamforming vectors are identically zero. This structural constraint will be explicitly incorporated in the subsequent optimization formulation.

In the k -th frame, the received signal at the u -th UT is

$$\begin{aligned} y_u^{(k)} &= \sum_{\ell \in \mathcal{L}^{(k)}} \mathbf{h}_{\ell,u}^{(k)\top} \mathbf{x}_\ell^{(k)} + n_u^{(k)} \\ &= \sum_{\ell \in \mathcal{L}^{(k)}} \mathbf{h}_{\ell,u}^{(k)\top} \mathbf{w}_{\ell,u}^{(k)} s_u^{(k)} + \underbrace{\sum_{i \neq u} \sum_{\ell \in \mathcal{L}^{(k)}} \mathbf{h}_{\ell,u}^{(k)\top} \mathbf{w}_{\ell,i}^{(k)} s_i^{(k)}}_{\text{Inter-user interference (IUI)}} + n_u^{(k)}, \end{aligned} \quad (2)$$

where $\mathbf{h}_{\ell,u}^{(k)} \in \mathbb{C}^N$ denote the channel vector from the ℓ -th satellite to the u -th UT and $n_u^{(k)} \sim \mathcal{CN}(0, \sigma^2)$ denotes the additive white Gaussian noise (AWGN), with variance $\sigma^2 = FN_0B$. Here, F denotes the noise figure, N_0 represents the single-sided power spectral density (PSD), and B is the system bandwidth.

B. LEO Channel Representation

We next specify $\mathbf{h}_{\ell,u}^{(k)}$. In the k -th frame, the multipath model between the ℓ -th satellite and the u -th UT at time t and frequency f is expressed by

$$\begin{aligned} \mathbf{h}_{\ell,u}^{(k)}(t, f) &= \sum_{m=0}^{M_{\ell,u}^{(k)}} \alpha_{\ell,u,m}^{(k)} G(\theta_{\ell,u,m}^{(k)\text{el}}) e^{j2\pi(t\tau_{\ell,u,m}^{(k)} - f\tau_{\ell,u,m}^{(k)})} \\ &\quad \times \mathbf{a}(\theta_{\ell,u,m}^{(k)}), \end{aligned} \quad (3)$$

where $M_{\ell,u}^{(k)}$ denotes the number of multipaths with $m=0$ denoting the LoS path and $m \geq 1$ being the non-line-of-sight (NLOS) paths, and $\alpha_{\ell,u,m}^{(k)}$ represents the complex channel gain associated with the m -th path. Here, the delay and Doppler of the m -th path are denoted by $\tau_{\ell,u,m}^{(k)}$ and $\nu_{\ell,u,m}^{(k)}$, respectively, and $\theta_{\ell,u,m}^{(k)} = [\theta_{\ell,u,m}^{(k)\text{az}}, \theta_{\ell,u,m}^{(k)\text{el}}]^\top$ is the angle-of-departure (AOD) while the elevation-only radiation pattern $G(\theta^{\text{el}})$ is boresight-symmetric [11], [15], [30]. Let $\mathbf{n}(N) = [0, \dots, N-1]^\top$. The steering vector is given by

$$\mathbf{a}(\theta_{\ell,u,m}^{(k)}) = e^{-j2\pi\phi_{\ell,u,m}^{(k)\text{h}} \mathbf{n}(N_h)} \otimes e^{-j2\pi\phi_{\ell,u,m}^{(k)\text{v}} \mathbf{n}(N_v)}, \quad (4)$$

with spatial frequencies $\phi_{\ell,u,m}^{(k)\text{h}} = d \cos \theta_{\ell,u,m}^{(k)\text{az}} \cos \theta_{\ell,u,m}^{(k)\text{el}} / \lambda$ and $\phi_{\ell,u,m}^{(k)\text{v}} = d \sin \theta_{\ell,u,m}^{(k)\text{az}} \cos \theta_{\ell,u,m}^{(k)\text{el}} / \lambda$, where d is the element spacing and λ is the carrier wavelength.

1) *LOS Approximation of LEO Channel*: Since LEO satellites are far above the local scattering region around each

UT, the path angles observed at the satellite array are highly concentrated. As a result, the directions of the multipaths are nearly identical, i.e., $\boldsymbol{\theta}_{\ell,u,m}^{(k)} \approx \boldsymbol{\theta}_{\ell,u}^{(k)}$ for all m . Moreover, by decomposing the Doppler shift into satellite- and UT-induced components as $v_{\ell,u,m}^{(k)} = v_{\ell,u,m}^{(k)\text{Sat}} + v_{\ell,u,m}^{(k)\text{UT}}$, the satellite-induced Doppler component dominates and is essentially common across multipaths, i.e., $v_{\ell,u,m}^{(k)\text{Sat}} \approx v_{\ell,u}^{(k)\text{Sat}}$ for all m .

Let $\tau_{\ell,u}^{(k)} = \tau_{\ell,u,0}^{(k)}$ denote the LoS delay and define the differential delays $\tau_{\ell,u,m}^{(k)\text{Diff}} = \tau_{\ell,u,m}^{(k)} - \tau_{\ell,u}^{(k)}$. With the above approximations, (3) can be rearranged into

$$\mathbf{h}_{\ell,u}^{(k)}(t, f) = \alpha_{\ell,u}^{(k)}(t, f) e^{j2\pi(t v_{\ell,u}^{(k)\text{Sat}} - f \tau_{\ell,u}^{(k)})} \mathbf{b}(\boldsymbol{\theta}_{\ell,u}^{(k)}), \quad (5)$$

where $\mathbf{b}(\boldsymbol{\theta}_{\ell,u}^{(k)}) = G(\boldsymbol{\theta}_{\ell,u}^{(k)\text{el}}) \mathbf{a}(\boldsymbol{\theta}_{\ell,u}^{(k)})$ accounts for the array response and the elevation-dependent antenna gain, and the effective complex channel gain is

$$\alpha_{\ell,u}^{(k)}(t, f) = \sum_{m=0}^{M_{\ell,u}^{(k)}} \alpha_{\ell,u,m}^{(k)} e^{j2\pi(t v_{\ell,u,m}^{(k)\text{UT}} - f \tau_{\ell,u,m}^{(k)\text{Diff}})}. \quad (6)$$

Under slow UT mobility and narrowband operation, $\alpha_{\ell,u}^{(k)}(t, f)$ varies slowly over time and is approximately flat over the signal bandwidth [11]. Hence, we drop the explicit (t, f) dependence and adopt a standard Rician model with Rician factor $\kappa_{\ell,u}^{(k)}$ and average power $\mathbb{E}[|\alpha_{\ell,u}^{(k)}|^2] = \gamma_{\ell,u}^{(k)}$ [7], [31]. Specifically, the real and imaginary parts of $\alpha_{\ell,u}^{(k)}$ are modeled as independent Gaussian random variables with mean $\bar{\alpha}_{\ell,u}^{(k)}$ and variance $\beta_{\ell,u}^{(k)}$ given by

$$\bar{\alpha}_{\ell,u}^{(k)} = \sqrt{\frac{\kappa_{\ell,u}^{(k)} \gamma_{\ell,u}^{(k)}}{2(1 + \kappa_{\ell,u}^{(k)})}}, \quad \beta_{\ell,u}^{(k)} = \frac{\gamma_{\ell,u}^{(k)}}{2(1 + \kappa_{\ell,u}^{(k)})}.$$

2) *Ephemeris-Aided Compensation*: By leveraging predictable satellite position and velocity (ephemeris information), the dominant delay and Doppler terms in (5) can be *pre-compensated at the transmitter* on a per-UT data-stream basis, i.e., each satellite applies a dedicated delay/Doppler pre-compensation to the stream intended for each UT prior to radiation [7], [16], [21], [31]. We note that such per-stream pre-compensation may induce asynchronous interference terms in a strict signal model (see, e.g., [12]). However, since this paper focuses on the handover-aware design layer, we adopt the standard ideal-compensation abstraction and leave the incorporation of these asynchrony effects to future work. Under this assumption, the effective channel used in (2) reduces to

$$\mathbf{h}_{\ell,u}^{(k)} = \alpha_{\ell,u}^{(k)} \mathbf{b}(\boldsymbol{\theta}_{\ell,u}^{(k)}). \quad (7)$$

III. HANDOVER-AWARE POWER CONSUMPTION AND COMMUNICATION PERFORMANCE METRICS

In this section, we introduce a handover-aware modeling layer for networked LEO systems. Specifically, we adopt a two-segment frame structure that separates handover-related operations from pure data transmission, and then define a corresponding handover-aware power consumption model and a statistical rate metric. These definitions provide the key ingredients for the joint design developed in Section IV.

A. Frame Structure

Due to the high orbital velocity of LEO satellites, the LEO-UT scheduling is inherently time-varying. To preserve link visibility and quality, each UT must periodically switch its serving satellites. Such scheduling updates inevitably trigger handover procedures, during which additional signaling, synchronization, and link re-establishment are required before stable user-plane data transmission can resume [4], [23]. For example, in the 3GPP NR-NTN framework [4, Sec. 16.14.2], when a handover to a new serving satellite/beam is triggered, the UT may need to perform a random access channel (RACH) procedure to acquire a valid timing advance and support Doppler-related synchronization. Although this procedure is specified for a single serving cell/beam, in a networked LEO setting the same requirement applies whenever the UT's *anchor* serving link (or any newly activated satellite-UT link) is established, while the remaining cooperating satellites coordinate data transmission via ISLs. Since LEO satellite visibility and geometry evolve rapidly, such handover-triggered procedures can occur frequently over time, depending on the beam footprint, handover policy, and user location. This procedure consumes dedicated physical random access channel (PRACH) resources within the radio frame and incurs additional transmission power for control-plane signaling.

Motivated by the NTN handover procedure specified in the 3GPP framework, we adopt the abstract frame structure shown in Fig. 2, which parallels the handover-and-transmission timeline commonly used in terrestrial systems [32]. Specifically, each frame is partitioned into two segments. The first segment is a handover-decision subframe occupying a fraction $\tau_{\text{HO}} \in (0, 1)$ of the frame, during which a handover may be triggered depending on whether a new LEO-UT scheduling is selected by the employed scheme. The remaining fraction $1 - \tau_{\text{HO}}$ is then dedicated to user-plane data transmission, operating either under the updated scheduling (if a handover occurs) or under the previous scheduling (otherwise).

B. Handover-Aware Power Consumption Model

Let $\delta_{\ell,u}^{(k)} = 1 + \{\|\mathbf{w}_{\ell,u}^{(k)}\|^2\}$ indicate whether the ℓ -th satellite serves the u -th UT in the k -th frame, where $1 + \{x\} = 1$ if $x > 0$ and $1 + \{x\} = 0$ otherwise. Equivalently, $\delta_{\ell,u}^{(k)} = 1$ if and only if the corresponding beamformer is nonzero.

The total power consumption of the ℓ -th satellite in the k -th frame is modeled as

$$P_{\ell}^{(k)} = \underbrace{\sum_{u=1}^U \left(\delta_{\ell,u}^{(k)} (1 - \delta_{\ell,u}^{(k-1)}) P_{\text{HO}} \right)}_{\text{Handover-related power}} + \underbrace{\tau_{\text{HO}} \left(\sum_{u=1}^U \left(\delta_{\ell,u}^{(k-1)} \|\mathbf{w}_{\ell,u}^{(k)}\|^2 + (1 - \tau_{\text{HO}}) \|\mathbf{w}_{\ell,u}^{(k)}\|^2 \right) \right)}_{\text{Radiated power}}, \quad (8)$$

where P_{HO} denotes an effective per-link handover overhead cost (energy-equivalent) associated with establishing a new satellite-UT link (e.g., access/synchronization/control signaling [4], [5]). Although this overhead is typically smaller than payload transmission power, it is nonzero and can accumulate

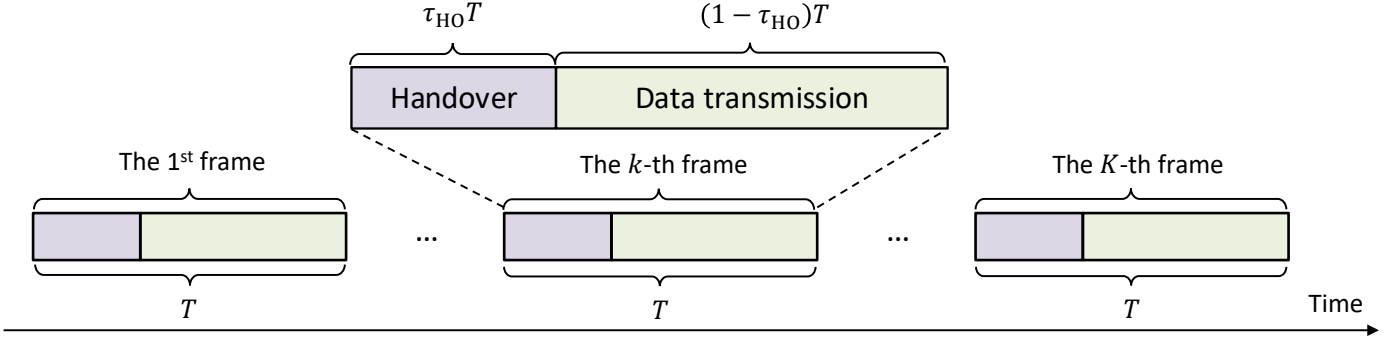


Fig. 2. Illustration of the considered frame structure for networked LEO satellite communications. Each frame has duration T . At the beginning of every frame, the serving satellite set $\mathcal{L}^{(k)}$ is re-evaluated and the joint cooperative beamforming and scheduling variables are updated. If the user scheduling differs from the previous frame, a handover procedure incurs a delay $\tau_{\text{HO}}T$, after which downlink data transmission proceeds for the remaining $(1 - \tau_{\text{HO}})T$.

under frequent LEO handovers. We therefore model it explicitly to capture its impact on the network power budget.

The handover-related term in (8) is activated only when a new scheduling is established, i.e., when $\delta_{\ell,u}^{(k-1)} = 0$ and $\delta_{\ell,u}^{(k)} = 1$. The radiated-power term reflects the two-segment frame structure in Fig. 2. Specifically, during the handover-decision subframe of duration fraction τ_{HO} , we assume that *newly scheduled* satellite-UT links are not yet available because handover signaling/synchronization is being performed on dedicated control resources, whereas user-plane transmission may continue on the *previously established* serving links (possibly from multiple satellites), captured by $\{\delta_{\ell,u}^{(k-1)}\}_{\forall \ell,u}$. This defines a partial-service-continuity (make-before-break-like) abstraction, motivated by reducing interruption time in highly dynamic LEO systems and conceptually aligned with source-link-maintaining handover mechanisms such as dual active protocol stack (DAPS) in NR [4, Sec. 9.2.3.2.2]. Although DAPS is not explicitly supported in the current NR-NTN specification, we use this as a generic modeling layer to capture possible overlap between handover signaling and continued transmission on already-established links (e.g., future protocol enhancements or implementation-specific mobility procedures). During the remaining fraction $1 - \tau_{\text{HO}}$, data transmission follows the scheduling selected for the current frame, captured by $\{\delta_{\ell,u}^{(k)}\}_{\forall \ell,u}$ through the beamformers $\{\mathbf{w}_{\ell,u}^{(k)}\}_{\forall \ell,u}$.

It is also worth noting that the cooperating satellite set \mathcal{L}_k is time-varying. Hence, some satellites may leave the serving set from the $(k-1)$ -th frame to the k -th frame, while new satellites may enter \mathcal{L}_k even though they were not in \mathcal{L}_{k-1} . Accordingly, when evaluating (8) in the k -th frame (with $\ell \in \mathcal{L}_k$), the previous-frame scheduling indicator $\delta_{\ell,u}^{(k-1)}$ is interpreted as follows: for satellites newly entering \mathcal{L}_k , we set

$$\delta_{\ell,u}^{(k-1)} = 0, \forall \ell \notin \mathcal{L}_k \cap \mathcal{L}_{k-1}. \quad (9)$$

The network-wide power consumption over the cooperating satellite set \mathcal{L}_k in the k -th frame is given by

$$P_{\text{total}}^{(k)} = \sum_{\ell \in \mathcal{L}_k} P_{\ell}^{(k)}. \quad (10)$$

C. Handover-Aware Communication Performance Metric

In LEO satellite systems, acquiring accurate instantaneous CSI can be challenging due to rapid channel variation in-

duced by satellite motion and non-negligible round-trip latency, especially when compared to terrestrial networks [33]–[37]. Motivated by these practical limitations, we evaluate communication performance using a statistical metric. Specifically, we adopt the hardening bound, a widely used lower bound on the ergodic rate that serves as a tractable performance proxy [28], [29].

In the k -th frame, define the effective beamformed gains across the cooperating satellites as $\mathbf{g}_{u,i}^{(k)} = [g_{1,u,i}^{(k)}, \dots, g_{\ell,u,i}^{(k)}]^T$, where

$$g_{\ell,u,i}^{(k)} = \mathbf{b}^T \left(\boldsymbol{\theta}_{\ell,u}^{(k)} \right) \mathbf{w}_{\ell,u}^{(k)}. \quad (11)$$

Moreover, stack the effective complex channel gains across satellites as $\boldsymbol{\alpha}_u^{(k)} = [\alpha_{1,u}^{(k)}, \dots, \alpha_{\ell,u}^{(k)}]^T$. With these definitions, the aggregated effective beamformed channel gain from the i -th data stream to the u -th UT in the k -th frame is

$$\Upsilon_{u,i}^{(k)} = \sum_{\ell \in \mathcal{L}^{(k)}} \alpha_{\ell,u}^{(k)} g_{\ell,u,i}^{(k)}. \quad (12)$$

Then, the hardening-bound ergodic downlink rate of the u -th UT is given by [11], [18], [21]

$$R_u^{(k)} = \log_2 \left(1 + \frac{|\mathbb{E}[\Upsilon_{u,u}^{(k)}]|^2}{\mathbb{V}[\Upsilon_{u,u}^{(k)}] + \sum_{i \neq u}^U \mathbb{E}[|\Upsilon_{u,i}^{(k)}|^2] + \sigma^2} \right). \quad (13)$$

By using the Rician parameterization in (7) and assuming independence of $\{\alpha_{\ell,u}^{(k)}\}_{\ell}$ across satellites (which is reasonable due to large inter-satellite separations), we obtain

$$\mathbb{E}[\Upsilon_{u,u}^{(k)}] = \sum_{\ell \in \mathcal{L}^{(k)}} \bar{\alpha}_{\ell,u}^{(k)} g_{\ell,u,u}^{(k)}, \quad (14a)$$

$$\mathbb{V}[\Upsilon_{u,u}^{(k)}] = \sum_{\ell \in \mathcal{L}^{(k)}} \beta_{\ell,u}^{(k)} |g_{\ell,u,u}^{(k)}|^2, \quad (14b)$$

$$\mathbb{E}[|\Upsilon_{u,i}^{(k)}|^2] = \mathbf{g}_{u,i}^{(k)H} \mathbf{T}_u^{(k)} \mathbf{g}_{u,i}^{(k)}. \quad (14c)$$

Here,

$$\mathbf{T}_u^{(k)} = \mathbb{E}[\boldsymbol{\alpha}_u^{(k)} \boldsymbol{\alpha}_u^{(k)H}] = \bar{\boldsymbol{\alpha}}_u^{(k)} \bar{\boldsymbol{\alpha}}_u^{(k)H} + \text{diag}(\boldsymbol{\beta}_u^{(k)}), \quad (15)$$

with $\bar{\boldsymbol{\alpha}}_u^{(k)} = [\bar{\alpha}_{1,u}^{(k)}, \dots, \bar{\alpha}_{\ell,u}^{(k)}]^T$ and $\boldsymbol{\beta}_u^{(k)} = [\beta_{1,u}^{(k)}, \dots, \beta_{\ell,u}^{(k)}]^T$. Note that (13)–(15) show that $R_u^{(k)}$ depends only on statistical channel parameters (i.e., $\bar{\boldsymbol{\alpha}}_u^{(k)}$ and $\boldsymbol{\beta}_u^{(k)}$), rather than instantaneous CSI.

Introducing the handover process at the beginning of each frame naturally leads to a segmented performance metric over the frame duration. Specifically, we consider the weighted ergodic rate across the two frame segments:

$$\bar{R}_u^{(k)} = \tau_{\text{HO}} \tilde{R}_u^{(k)} + (1 - \tau_{\text{HO}}) R_u^{(k)}, \quad (16)$$

where $\tilde{R}_u^{(k)}$ corresponds to the handover-decision subframe (duration fraction τ_{HO}), while $R_u^{(k)}$ corresponds to the subsequent data-transmission subframe (duration fraction $1 - \tau_{\text{HO}}$). This segmentation is an abstraction of the NR time-frequency grid: access/handover signaling (e.g., PRACH/RACH) occupies dedicated time-frequency resources, while user-plane data for already-established links can still be scheduled on the remaining resources. Accordingly, during the τ_{HO} portion we allow payload transmission only on previously established links (and set newly activated links to be unavailable), whereas the $1 - \tau_{\text{HO}}$ portion represents the interval after the new links become usable for data.

The rate $\tilde{R}_u^{(k)}$ is obtained analogously to $R_u^{(k)}$ by replacing the effective beamformed gain $g_{\ell,u,i}^{(k)}$ in (14) with

$$\tilde{g}_{\ell,u,i}^{(k)} = \mathbf{b}^\top \left(\boldsymbol{\theta}_{\ell,u}^{(k)} \right) \delta_{\ell,u}^{(k-1)} \mathbf{w}_{\ell,i}^{(k)}. \quad (17)$$

Remark 1. *The proposed handover-aware power consumption model explicitly captures how handover events, user-scheduling decisions, and power consumption are intertwined through $\{P_\ell^{(k)}\}_{\ell \in \mathcal{L}_k}$. Specifically, LEO satellite systems inherently require frequent changes in user scheduling due to rapid topology variations. Consequently, if the handover-related power cost is decoupled from the scheduling dynamics (or ignored altogether), the resulting assessment of the system's energy efficiency can be overly optimistic. This motivates a joint optimization of user scheduling and beamforming under the proposed power consumption model.*

IV. HANDOVER-AWARE JOINT COOPERATIVE BEAMFORMING AND USER SCHEDULING

Building on the handover-aware power and rate metrics in Section III, this section formulates a per-frame network-wide power minimization problem with joint cooperative beamforming and LEO-UT scheduling under segmented QoS constraints. We develop an iterative solution by (i) converting the hardening-bound rate constraints into tractable convex forms (with separate treatments for $k = 1$ and $k > 1$), (ii) handling the scheduling-induced sparsity via a reweighted l_2 approximation, and (iii) employing an FP-based inner loop for the $k > 1$ case to address the resulting fractional structure.

A. Problem Formulation

In each frame, we aim to minimize the network-wide power consumption by jointly optimizing cooperative beamforming and LEO-UT scheduling in a handover-aware manner. For the k -th frame, the design problem is

$$\min_{\{\mathbf{w}_{\ell,u}^{(k)}\}_{\forall \ell,u}} P_{\text{total}}^{(k)} \quad (18a)$$

$$\text{s.t. } \tau_{\text{HO}} \tilde{R}_u^{(k)} + (1 - \tau_{\text{HO}}) R_u^{(k)} \geq \bar{R}_u, \quad \forall u, \quad (18b)$$

$$\sum_{u=1}^U 1_{+\{\|\mathbf{w}_{\ell,u}^{(k)}\|^2\}} \leq U_{\text{max}}, \quad \forall \ell, \quad (18c)$$

$$\sum_{u=1}^U \|\mathbf{w}_{\ell,u}^{(k)}\|^2 \leq P_{\text{rad}}, \quad \forall \ell. \quad (18d)$$

Here, P_{rad} is the maximum radiated power per satellite, (18b) enforces the QoS requirement for each UT with a minimum rate of \bar{R}_u , and (18c) limits each satellite to serving at most U_{max} UTs, thereby inducing user scheduling. Although the beamformers $\{\mathbf{w}_{\ell,u}^{(k)}\}_{\forall \ell,u}$ are the explicit optimization variables, the scheduling decisions are implicitly determined by which beamformers are nonzero, as captured by $1_{+\{\|\mathbf{w}_{\ell,u}^{(k)}\|^2\}}$.

It can be observed that (18) is challenging to solve for several reasons. First, user scheduling is inherently combinatorial due to the indicator functions in (18c), which enforce per-satellite serving-cardinality constraints through the sparsity pattern of the beamformers. Second, the QoS constraints are nonconvex because they are defined in terms of statistical-rate expressions (via the hardening bound), which couple the beamformers across satellites and users. Moreover, the handover-aware formulation introduces inter-frame coupling: the current-frame design depends on the previous-frame scheduling $\delta_{\ell,u}^{(k-1)}$ through (17) and the power consumption model, complicating both feasibility analysis and algorithm development.

B. Transformation of Sparsity Constraint

The per-satellite serving-cardinality constraint (18c) is nonconvex because it enforces sparsity on $\{\mathbf{w}_{\ell,u}^{(k)}\}_{\forall \ell,u}$. To obtain a tractable formulation, we employ a reweighted l_2 -norm approximation [38], [39].

Introduce an auxiliary power weight $\omega_{\ell,u}^{(k)}$ for each beamformer and impose

$$\|\mathbf{w}_{\ell,u}^{(k)}\| \leq \omega_{\ell,u}^{(k)} \sqrt{P_{\text{rad}}}, \quad \forall \ell, u, \quad (19)$$

which, together with (18d), implies

$$0 \leq \omega_{\ell,u}^{(k)} \leq 1, \quad \forall \ell, u. \quad (20)$$

Intuitively, $\omega_{\ell,u}^{(k)}$ quantifies the relative power portion allocated to the u -th UT at the ℓ -th satellite. We then detach the sparsity indicator from the beamformers by replacing $1_{+\{\|\mathbf{w}_{\ell,u}^{(k)}\|^2\}}$ with $1_{+\{\omega_{\ell,u}^{(k)}\}}$, which yields

$$\sum_{u=1}^U 1_{+\{\omega_{\ell,u}^{(k)}\}} \leq U_{\text{max}}, \quad \forall \ell. \quad (21)$$

To handle the remaining nonconvexity in (21), we introduce reweighting coefficients $\{z_{\ell,u}^{(k)}\}$ and approximate $1_{+\{\omega_{\ell,u}^{(k)}\}}$ with a weighted quadratic surrogate. Specifically, we adopt an iterative reweighting rule that updates $z_{\ell,u}^{(k)}$ based on the previous iterate. Given $\tilde{\omega}_{\ell,u}^{(k)}$ from the last iteration, we set

$$z_{\ell,u}^{(k)} = \frac{1}{\tilde{\omega}_{\ell,u}^{(k)2} + \epsilon}, \quad \forall \ell, u, \quad (22)$$

where $\epsilon > 0$ is a small constant used to avoid numerical issues when $\tilde{\omega}_{\ell,u}^{(k)}$ is close to zero. Then we employ the approximation

$$1_{+\{\omega_{\ell,u}^{(k)}\}} \approx z_{\ell,u}^{(k)} \omega_{\ell,u}^{(k)2}, \quad \forall \ell, u, \quad (23)$$

which leads to the a convex surrogate of (21) as

$$\sum_{u=1}^U z_{\ell,u}^{(k)} \omega_{\ell,u}^{(k)2} \leq U_{\max}, \forall \ell. \quad (24)$$

Remark 2. The reweighted l_2 -norm approximation replaces the indicator $1_{\{\omega_{\ell,u}^{(k)}\}}$ with the weighted quadratic term $z_{\ell,u}^{(k)} \omega_{\ell,u}^{(k)2}$. Since $z_{\ell,u}^{(k)}$ increases as $\omega_{\ell,u}^{(k)}$ decreases, the iterative reweighting imposes a stronger penalty on small power weights, pushing them toward zero and thereby promoting sparsity in $\{\omega_{\ell,u}^{(k)}\}_{\forall u}$.

Enforcing (24) strictly at every iteration, although convex, can lead to premature infeasibility during the reweighting process. This typically occurs when some $\omega_{\ell,u}^{(k)}$ become very small, causing the corresponding $z_{\ell,u}^{(k)}$ to grow excessively large. To improve numerical robustness, we adopt a penalty method by introducing a slack variable $\zeta_{\ell}^{(k)}$ and penalizing constraint violations in the objective [40], [41]. Specifically, (18) is relaxed as

$$\min_{\{\mathbf{w}_{\ell,u}^{(k)}, \omega_{\ell,u}^{(k)}, \zeta_{\ell}^{(k)}\}_{\forall \ell, u}} P_{\text{total}}^{(k)} + \mu \zeta_{\ell}^{(k)} \quad (25a)$$

$$\text{s.t. } \tau_{\text{HO}} \tilde{R}_u^{(k)} + (1 - \tau_{\text{HO}}) R_u^{(k)} \geq \bar{R}_u, \forall u, \quad (25b)$$

$$\sum_{u=1}^U z_{\ell,u}^{(k)} \omega_{\ell,u}^{(k)2} - U_{\max} \leq \zeta_{\ell}^{(k)}, \forall \ell, \quad (25c)$$

$$\|\mathbf{w}_{\ell,u}^{(k)}\| \leq \omega_{\ell,u}^{(k)} \sqrt{P_{\text{rad}}}, \forall \ell, u, \quad (25d)$$

$$\sum_{u=1}^U \|\mathbf{w}_{\ell,u}^{(k)}\|^2 \leq P_{\text{rad}}, \forall \ell. \quad (25e)$$

where μ is a penalty coefficient that controls how strongly violations of the relaxed constraint are discouraged. Following [40], μ is gradually increased across iterations by multiplying it by a constant $\rho > 1$, i.e., $\mu \leftarrow \min\{\rho\mu, \mu_{\max}\}$, where μ_{\max} is a prescribed upper bound to avoid numerical issues. When μ becomes sufficiently large, $\zeta_{\ell}^{(k)}$ is driven close to zero, thereby effectively enforcing the original constraint (23).

C. Transformation of QoS Constraint

We next address the nonconvex QoS constraint. For the initial frame ($k = 1$), we initialize the system with no established schedulings by setting $\delta_{\ell,u}^{(0)} = 0$. Consequently, no data transmission is assumed during the handover-decision subframe of the first frame, yielding $\tilde{R}_u^{(1)} = 0$. Therefore, (18b) reduces to a single-rate constraint without the weighted two-segment structure. In the sequel, we handle (18b) by considering the cases $k = 1$ and $k > 1$ separately.

1) *Case $k = 1$:* When $k = 1$, the weighted two-segment QoS structure in (18b) reduces to a single rate constraint since no scheduling exists in the previous frame. As a result, (18b) becomes

$$R_u^{(1)} \geq \frac{\bar{R}_u}{1 - \tau_{\text{HO}}}, \forall u. \quad (26)$$

Note that (26) is still a nonconvex constraint because $R_u^{(1)}$ contains a quadratic-over-quadratic signal-to-interference-plus-noise ratio (SINR) term. Nevertheless, in the sequel, we

reveal that it admits an equivalent second-order cone (SOC) representation. Define

$$\eta_u = 2^{\bar{R}_u / (1 - \tau_{\text{HO}})} - 1, \quad (27)$$

and the stacked gain vector $\mathbf{g}_u^{(1)} = [\mathbf{g}_{u,1}^{(1)\top}, \dots, \mathbf{g}_{u,U}^{(1)\top}]^\top$. Then (26) is equivalent to

$$\frac{\left| \sum_{\ell \in \mathcal{L}^{(1)}} \bar{\alpha}_{\ell,u}^{(1)} g_{\ell,u,u}^{(1)} \right|^2}{\mathbf{g}_u^{(1)\text{H}} \boldsymbol{\Omega}_u^{(1)} \mathbf{g}_u^{(1)} + \sigma^2} \geq \eta_u, \forall u, \quad (28)$$

with

$$\boldsymbol{\Omega}_u^{(1)} = \text{diag} \left(\mathbf{T}_u^{(1)}, \dots, \underbrace{\mathbf{Q}_u^{(1)}}_{u\text{-th block}}, \dots, \mathbf{T}_u^{(1)} \right), \quad (29)$$

and $\mathbf{Q}_u^{(1)} = \text{diag}([\beta_{\ell,u}^{(1)}]_{\forall \ell \in \mathcal{L}^{(1)}})$.

Moreover, a *common* phase rotation can be applied to $\{\mathbf{w}_{\ell,u}^{(1)}\}_{\forall \ell \in \mathcal{L}^{(1)}}$ (and hence to $\{g_{\ell,u,u}^{(1)}\}_{\forall \ell \in \mathcal{L}^{(1)}}$) without changing either the objective or the constraints. Therefore, without loss of optimality, we impose

$$\Re \left\{ \sum_{\ell \in \mathcal{L}^{(1)}} \bar{\alpha}_{\ell,u}^{(1)} g_{\ell,u,u}^{(1)} \right\} \geq 0, \forall u, \quad (30a)$$

$$\Im \left\{ \sum_{\ell \in \mathcal{L}^{(1)}} \bar{\alpha}_{\ell,u}^{(1)} g_{\ell,u,u}^{(1)} \right\} = 0, \forall u. \quad (30b)$$

With (30), (28) can be equivalently written in SOC form as

$$\left\| \boldsymbol{\Psi}_u^{(1)} \mathbf{g}_u^{(1)} + \mathbf{v}_u \right\| \leq \frac{1}{\sqrt{\eta_u}} \sum_{\ell \in \mathcal{L}^{(1)}} \bar{\alpha}_{\ell,u}^{(1)} g_{\ell,u,u}^{(1)}, \forall u, \quad (31)$$

where $\mathbf{v}_u = [\mathbf{0}_{SU}^\top, \sigma]^\top$ and $\boldsymbol{\Psi}_u^{(1)}$ satisfies $\boldsymbol{\Omega}_u^{(1)} = \boldsymbol{\Psi}_u^{(1)\text{H}} \boldsymbol{\Psi}_u^{(1)}$ (e.g., a Cholesky factor). Such a factorization is always well-defined because $\mathbf{T}_u^{(1)} = \mathbb{E}[\boldsymbol{\alpha}_u^{(1)} \boldsymbol{\alpha}_u^{(1)\text{H}}]$ is Hermitian positive semidefinite and $\mathbf{Q}_u^{(1)}$ has nonnegative diagonal entries, implying that $\boldsymbol{\Omega}_u^{(1)}$ is Hermitian positive semidefinite. Additionally, (30b) becomes redundant since it can be ensured via (31).

2) *Case $k > 1$:* When $k > 1$, we first decouple the weighted two-segment QoS constraint in (18b) by introducing auxiliary variables $\tilde{\Gamma}_u^{(k)}$ and $\Gamma_u^{(k)}$, yielding

$$\tau_{\text{HO}} \tilde{\Gamma}_u^{(k)} + (1 - \tau_{\text{HO}}) \Gamma_u^{(k)} \geq \bar{R}_u, \forall u, \quad (32)$$

$$\tilde{R}_u^{(k)} \geq \tilde{\Gamma}_u^{(k)}, \forall u, \quad (33)$$

$$R_u^{(k)} \geq \Gamma_u^{(k)}, \forall u. \quad (34)$$

Accordingly, it remains to handle the nonconvex constraints (33) and (34).

To this end, through algebraic manipulation and by applying the phase-rotation technique introduced earlier, we reformulate (33) and (34) as

$$\frac{\left(\sum_{\ell \in \mathcal{L}^{(k)}} \bar{\alpha}_{\ell,u}^{(k)} \tilde{g}_{\ell,u,u}^{(k)} \right)^2}{\tilde{\mathbf{g}}_u^{(k)\text{H}} \tilde{\boldsymbol{\Omega}}_u^{(k)} \tilde{\mathbf{g}}_u^{(k)} + \sigma^2} \geq 2\tilde{\Gamma}_u^{(k)} - 1, \forall u, \quad (35a)$$

$$\Re \left\{ \sum_{\ell \in \mathcal{L}^{(k)}} \bar{\alpha}_{\ell,u}^{(k)} \tilde{g}_{\ell,u,u}^{(k)} \right\} \geq 0, \forall u, \quad (35b)$$

$$\Im \left\{ \sum_{\ell \in \mathcal{L}^{(k)}} \bar{\alpha}_{\ell,u}^{(k)} \tilde{g}_{\ell,u,u}^{(k)} \right\} = 0, \forall u, \quad (35c)$$

and

$$\frac{\left(\sum_{\ell \in \mathcal{L}^{(k)}} \bar{\alpha}_{\ell,u}^{(k)} \tilde{g}_{\ell,u,u}^{(k)} \right)^2}{\mathbf{g}_u^{(k)H} \mathbf{\Omega}_u^{(k)} \mathbf{g}_u^{(k)} + \sigma^2} \geq 2^{\Gamma_u^{(k)}} - 1, \forall u, \quad (36a)$$

$$\Re \left\{ \sum_{\ell \in \mathcal{L}^{(k)}} \bar{\alpha}_{\ell,u}^{(k)} \tilde{g}_{\ell,u,u}^{(k)} \right\} \geq 0, \forall u, \quad (36b)$$

$$\Im \left\{ \sum_{\ell \in \mathcal{L}^{(k)}} \bar{\alpha}_{\ell,u}^{(k)} \tilde{g}_{\ell,u,u}^{(k)} \right\} = 0, \forall u, \quad (36c)$$

respectively, where the stacked gain vectors $\tilde{\mathbf{g}}_u^{(k)} = [\tilde{\mathbf{g}}_{u,1}^{(k)T}, \dots, \tilde{\mathbf{g}}_{u,U}^{(k)T}]^T$ and $\mathbf{g}_u^{(k)} = [\mathbf{g}_{u,1}^{(k)T}, \dots, \mathbf{g}_{u,U}^{(k)T}]^T$.

To circumvent the nonconvex fractional structures in (35) and (36), we employ the FP technique introduced in [42]–[44]. Specifically, using the equivalence in [42], [43], we transform (35a) and (36a) into

$$\begin{aligned} \max_{\tilde{\lambda}_u^{(k)}} 2\tilde{\lambda}_u^{(k)} \left(\sum_{\ell \in \mathcal{L}^{(k)}} \bar{\alpha}_{\ell,u}^{(k)} \tilde{g}_{\ell,u,u}^{(k)} \right) - \tilde{\lambda}_u^{(k)2} \left(\tilde{\mathbf{g}}_u^{(k)H} \mathbf{\Omega}_u^{(k)} \tilde{\mathbf{g}}_u^{(k)} + \sigma^2 \right) \\ \geq 2^{\tilde{\Gamma}_u^{(k)}} - 1, \forall u, \end{aligned} \quad (37)$$

and

$$\begin{aligned} \max_{\lambda_u^{(k)}} 2\lambda_u^{(k)} \left(\sum_{\ell \in \mathcal{L}^{(k)}} \bar{\alpha}_{\ell,u}^{(k)} \tilde{g}_{\ell,u,u}^{(k)} \right) - \lambda_u^{(k)2} \left(\mathbf{g}_u^{(k)H} \mathbf{\Omega}_u^{(k)} \mathbf{g}_u^{(k)} + \sigma^2 \right) \\ \geq 2^{\Gamma_u^{(k)}} - 1, \forall u, \end{aligned} \quad (38)$$

respectively, where $\tilde{\lambda}_u^{(k)}$ and $\lambda_u^{(k)}$ are the introduced auxiliary variables. Moreover, (35b) and (36b) are inherently satisfied when (37) and (38) hold, respectively.

It should be emphasized that (37) and (38) have a “less-than-max” structure, which allows $\tilde{\lambda}_u^{(k)}$ and $\lambda_u^{(k)}$ to be treated via an inner-iteration procedure. Specifically, for fixed $\mathbf{w}_{\ell,u}^{(k)}$ (and thus fixed $\tilde{g}_{\ell,u,i}^{(k)}$ and $g_{\ell,u,i}^{(k)}$), the optimal auxiliary variables are updated as [42], [43]

$$\tilde{\lambda}_u^{(k)} = \frac{\sum_{\ell \in \mathcal{L}^{(k)}} \bar{\alpha}_{\ell,u}^{(k)} \tilde{g}_{\ell,u,u}^{(k)}}{\tilde{\mathbf{g}}_u^{(k)H} \mathbf{\Omega}_u^{(k)} \tilde{\mathbf{g}}_u^{(k)} + \sigma^2}, \forall u, \quad (39)$$

and

$$\lambda_u^{(k)} = \frac{\left(\sum_{\ell \in \mathcal{L}^{(k)}} \bar{\alpha}_{\ell,u}^{(k)} \tilde{g}_{\ell,u,u}^{(k)} \right)^2}{\mathbf{g}_u^{(k)H} \mathbf{\Omega}_u^{(k)} \mathbf{g}_u^{(k)} + \sigma^2}, \forall u, \quad (40)$$

respectively.

D. Overall Procedure

By combining the above transformations, we solve (18) in an iterative manner. The resulting procedure depends on whether $k = 1$ or $k > 1$.

1) *Case $k = 1$* : At each iteration, given $z_{\ell,u}^{(1)}$, we compile (25) with the convex constraints (30b) and (31), and solve

$$\min_{\{\mathbf{w}_{\ell,u}^{(1)}, \omega_{\ell,u}^{(1)}, \zeta_{\ell}^{(1)}\}_{\forall \ell, u}} P_{\text{total}}^{(k)} + \mu \zeta_{\ell}^{(1)} \quad (41a)$$

Algorithm 1 Proposed Handover-Aware Joint Cooperative Beamforming and User Scheduling

Input: $\{\bar{\alpha}_{\ell,u}^{(k)}, \beta_{\ell,u}^{(k)}, \mathbf{b}(\boldsymbol{\theta}_{\ell,u}^{(k)}), \mathcal{L}^{(k)}\}_{\forall \ell, u, k}$, τ_{HO} , U_{max} , P_{rad} , P_{HO} , σ^2 , ϵ , ρ , and $\mu = \mu_0$.

- 1: **Initialize:** $\{\mathbf{w}_{\ell,u}^{(1)}, \tilde{\omega}_{\ell,u}^{(1)}, z_{\ell,u}^{(1)}\}_{\forall \ell, u}$.
- 2: **for** $k = 1 : K$ **do**
- 3: **if** $k = 1$ (*Initial frame*) **then**
- 4: **repeat** (*Loop: reweighted l_2 approximation*)
- 5: Solve (41) via CVX.
- 6: Update $z_{\ell,u}^{(1)}$ using (22).
- 7: Update $\mu \leftarrow \min\{\rho\mu, \mu_{\text{max}}\}$.
- 8: **until** the relative change of $P_{\text{total}}^{(1)}$ falls below a threshold or a maximum number of iterations is reached.
- 9: Set $\delta_{\ell,u}^{(1)} = 1 + \{\|\mathbf{w}_{\ell,u}^{(1)}\|^2\}$ for all $\ell \in \mathcal{L}^{(1)}$ and u .
- 10: **else** (*Subsequent frames*)
- 11: Initialize $\{\mathbf{w}_{\ell,u}^{(k)}, \tilde{\omega}_{\ell,u}^{(k)}, z_{\ell,u}^{(k)}\}_{\forall \ell, u}$ and set $\mu = \mu_0$.
- 12: **repeat** (*Outer loop: reweighted l_2 approximation*)
- 13: Initialize $\{\tilde{\lambda}_u^{(k)}, \lambda_u^{(k)}\}_{\forall u}$ via (39) and (40).
- 14: **repeat** (*Inner loop: FP process*)
- 15: Solve (42) via CVX.
- 16: Update $\{\tilde{\lambda}_u^{(k)}, \lambda_u^{(k)}\}_{\forall u}$ via (39) and (40).
- 17: **until** the relative change of $P_{\text{total}}^{(k)}$ falls below a threshold or a maximum number of iterations is reached.
- 18: Update $z_{\ell,u}^{(k)}$ using (22).
- 19: Update $\mu \leftarrow \min\{\rho\mu, \mu_{\text{max}}\}$.
- 20: **until** the relative change of $P_{\text{total}}^{(k)}$ falls below a threshold or a maximum number of iterations is reached.
- 21: Set $\delta_{\ell,u}^{(k)} = 1 + \{\|\mathbf{w}_{\ell,u}^{(k)}\|^2\}$ for all $\ell \in \mathcal{L}^{(k)}$ and u .
- 22: **end if**
- 23: **end for**
- 24: **Output:** $\{\mathbf{w}_{\ell,u}^{(k)}\}$ and $\{\delta_{\ell,u}^{(k)}\}$.

$$\text{s.t. } \left\| \Psi_u^{(1)} \mathbf{g}_u^{(1)} + \mathbf{v}_u \right\| \leq \frac{1}{\sqrt{\eta_u}} \sum_{\ell \in \mathcal{L}^{(1)}} \bar{\alpha}_{\ell,u}^{(1)} g_{\ell,u,u}^{(1)}, \forall u, \quad (41b)$$

$$\Im \left\{ \sum_{\ell \in \mathcal{L}^{(1)}} \bar{\alpha}_{\ell,u}^{(1)} g_{\ell,u,u}^{(1)} \right\} = 0, \forall u, \quad (41c)$$

$$\sum_{u=1}^U z_{\ell,u}^{(1)} \omega_{\ell,u}^{(1)2} - U_{\text{max}} \leq \zeta_{\ell}^{(1)}, \forall \ell, \quad (41d)$$

$$\left\| \mathbf{w}_{\ell,u}^{(1)} \right\| \leq \omega_{\ell,u}^{(1)} \sqrt{P_{\text{rad}}}, \forall \ell, u, \quad (41e)$$

$$\sum_{u=1}^U \left\| \mathbf{w}_{\ell,u}^{(1)} \right\|^2 \leq P_{\text{rad}}, \forall \ell. \quad (41f)$$

Note that (41) is convex and can be solved using a standard tool such as CVX. After solving it, the resulting $\omega_{\ell,u}^{(1)}$ are used to update $z_{\ell,u}^{(1)}$ via (22), and the above steps are repeated until convergence.

2) *Case $k > 1$* : When $k > 1$, the FP-based reformulation introduces an additional set of auxiliary variables, which leads to a double-loop procedure. Specifically, in each outer iteration, we fix $z_{\ell,u}^{(k)}$. Then, within the corresponding inner iteration, we fix $\tilde{\lambda}_u^{(k)}$ and $\lambda_u^{(k)}$, and solve a convex subproblem formed by compiling (25) with (32), (35a), (35b), (36a), and (36b),

expressed as

$$\min_{\{\mathbf{w}_{\ell,u}^{(k)}, \omega_{\ell,u}^{(k)}, \tilde{\lambda}_u^{(k)}, \lambda_u^{(k)}, \zeta_\ell^{(k)}\}_{\forall \ell, u}} P_{\text{total}}^{(k)} + \mu \zeta_\ell^{(k)} \quad (42a)$$

$$\text{s.t. } \tau_{\text{HO}} \tilde{\Gamma}_u^{(k)} + (1 - \tau_{\text{HO}}) \Gamma_u^{(k)} \geq \bar{R}_u, \forall u, \quad (42b)$$

$$2\tilde{\lambda}_u^{(k)} \left(\sum_{\ell \in \mathcal{L}^{(k)}} \bar{\alpha}_{\ell,u}^{(k)} \tilde{g}_{\ell,u,u}^{(k)} \right) - \tilde{\lambda}_u^{(k)2} \left(\tilde{\mathbf{g}}_u^{(k)\text{H}} \mathbf{\Omega}_u^{(k)} \tilde{\mathbf{g}}_u^{(k)} + \sigma^2 \right) \geq 2\tilde{\Gamma}_u^{(k)} - 1, \forall u, \quad (42c)$$

$$2\lambda_u^{(k)} \left(\sum_{\ell \in \mathcal{L}^{(k)}} \bar{\alpha}_{\ell,u}^{(k)} g_{\ell,u,u}^{(k)} \right) - \lambda_u^{(k)2} \left(\mathbf{g}_u^{(k)\text{H}} \mathbf{\Omega}_u^{(k)} \mathbf{g}_u^{(k)} + \sigma^2 \right) \geq 2\Gamma_u^{(k)} - 1, \forall u, \quad (42d)$$

$$\Im \left\{ \sum_{\ell \in \mathcal{L}^{(k)}} \bar{\alpha}_{\ell,u}^{(k)} \tilde{g}_{\ell,u,u}^{(k)} \right\} = 0, \forall u, \quad (42e)$$

$$\Im \left\{ \sum_{\ell \in \mathcal{L}^{(k)}} \bar{\alpha}_{\ell,u}^{(k)} g_{\ell,u,u}^{(k)} \right\} = 0, \forall u, \quad (42f)$$

$$\sum_{u=1}^U z_{\ell,u}^{(k)} \omega_{\ell,u}^{(k)2} - U_{\text{max}} \leq \zeta_\ell^{(k)}, \forall \ell, \quad (42g)$$

$$\|\mathbf{w}_{\ell,u}^{(k)}\| \leq \omega_{\ell,u}^{(k)} \sqrt{P_{\text{rad}}}, \forall \ell, u, \quad (42h)$$

$$\sum_{u=1}^U \|\mathbf{w}_{\ell,u}^{(k)}\|^2 \leq P_{\text{rad}}, \forall \ell. \quad (42i)$$

We can see that (42) is convex for fixed $z_{\ell,u}^{(k)}$, $\tilde{\lambda}_u^{(k)}$, and $\lambda_u^{(k)}$. After each inner-iteration solve via CVX, the resulting $\mathbf{w}_{\ell,u}^{(k)}$ are used to update $\tilde{\lambda}_u^{(k)}$ and $\lambda_u^{(k)}$ via (39) and (40), respectively, and the inner loop repeats until convergence. After the inner loop converges, the resulting $\omega_{\ell,u}^{(k)}$ are used in the outer loop to update $z_{\ell,u}^{(k)}$ via (22), and the overall double-loop procedure repeats until convergence.

3) *Complexity Analysis*: The overall procedure for solving (18) using the proposed handover-aware joint cooperative beamforming and user scheduling algorithm is summarized in Algorithm 1. In each outer/inner iteration, the corresponding subproblem (i.e., (41) for $k = 1$ and (42) for $k > 1$) is an SOCP and is solved via an interior-point method. It is well known that the worst-case complexity of solving an SOCP scales as $\mathcal{O}(n^{3.5})$, where n is the dimension of the optimization variable. In our case, the dominant variables are the beamformers $\{\mathbf{w}_{\ell,u}^{(k)}\}_{\forall \ell, u}$, whose total dimension scales as $\mathcal{O}(|\mathcal{L}^{(k)}|UN)$. Therefore, the per-frame complexity scales as $\mathcal{O}(N_{\text{rw}}(|\mathcal{L}^{(1)}|UN)^{3.5})$ for $k = 1$, and as $\mathcal{O}(N_{\text{rw}}N_{\text{fp}}(|\mathcal{L}^{(k)}|UN)^{3.5})$ for $k > 1$, where N_{rw} and N_{fp} denote the maximum numbers of outer reweighting iterations and inner FP iterations, respectively.

V. NUMERICAL RESULTS

We consider a time-varying LEO downlink scenario. The Earth is modeled as a sphere with radius 6371 km, and the satellites operate at an orbital altitude of 590 km. We adopt

TABLE I
DEFAULT SIMULATION PARAMETERS

Parameter	Value
Carrier frequency f_c	12 GHz [47]
Signal bandwidth B	250 MHz [5], [47]
Noise PSD N_0	-173.855 dBm/Hz
Noise figure F	4 dB
Number of (selected) LEO satellites L	8
Number of UTs in the service set U	12
UPA size $N = N_h \times N_v$	4×4
Per-satellite maximum served users U_{max}	4
Per-satellite power budget P_{rad}	70 dBm
Handover power cost P_{HO}	50 dBm
Handover fraction τ_{HO}	0.2
Minimum rate requirement \bar{R}_u	0.05 bps/Hz
Frame number K	6
Frame duration	30 s
Radiation gain (amplitude) $G(\theta)$	$\sqrt{\frac{3}{2\pi}} \cos(\theta)$ [30]

maritime user data from [45]. The satellite constellation follows a Walker-Delta configuration with 28 orbit planes and 28 satellites per plane, and an orbital inclination of 53° [12], [46]. A fixed service center is located at latitude 25° and longitude -85° . The U closest UTs to the service center are selected and treated as static in the Earth-fixed coordinate system over the considered horizon. To capture topology evolution and satellite membership changes, we adopt a snapshot-based model with K frames, each lasting 30 s. Each satellite is equipped with a $N_h \times N_v$ UPA. To visualize the frame-wise evolution of the serving satellite set induced by LEO orbital motion, Fig. 3 shows representative topology snapshots across 4 consecutive frames. For each frame, the large-scale path loss $\gamma_{\ell,u}^{(k)}$ between satellite $\ell \in \mathcal{L}^{(k)}$ and user u is generated according to [5], [11]. The Rician factor $\kappa_{\ell,u}^{(k)}$ of each satellite-UT link is independently drawn from [15, 20] dB [5], [21]. Unless stated otherwise, all key parameters are summarized in Table I.

A. Benchmark Schemes

1) *Cooperative Beamforming with Pre-fixed Scheduling*: To isolate the gain from *joint* scheduling and cooperative beamforming, we benchmark against pragmatic *pre-fixed* scheduling rules. In these baselines, the binary variables $\{\delta_{\ell,u}^{(k)}\}_{\forall \ell, u}$ are determined *prior* to beamforming, independently at each frame, subject to the per-satellite serving-capacity constraint. All rules follow the same two-stage procedure for a fair comparison. In Stage (i), we ensure that each UT is associated with at least one satellite (otherwise the QoS constraint is infeasible). In Stage (ii), any remaining per-satellite capacity is used to add *extra cooperative links* according to each rule.

- **Random-generated**: In Stage (i), for each UT, one satellite is selected uniformly at random and we set $\delta_{\ell,u}^{(k)} = 1$ for that pair. In Stage (ii), for each satellite with remaining capacity, additional UTs are sampled uniformly at random (excluding already-associated pairs) until $\sum_{u=1}^U \delta_{\ell,u}^{(k)} = U_{\text{max}}$ or no candidates remain.
- **Distance-based**: In Stage (i), each UT is assigned to its nearest satellite with remaining capacity, i.e., the feasible satellite minimizing distance. This yields a coverage-

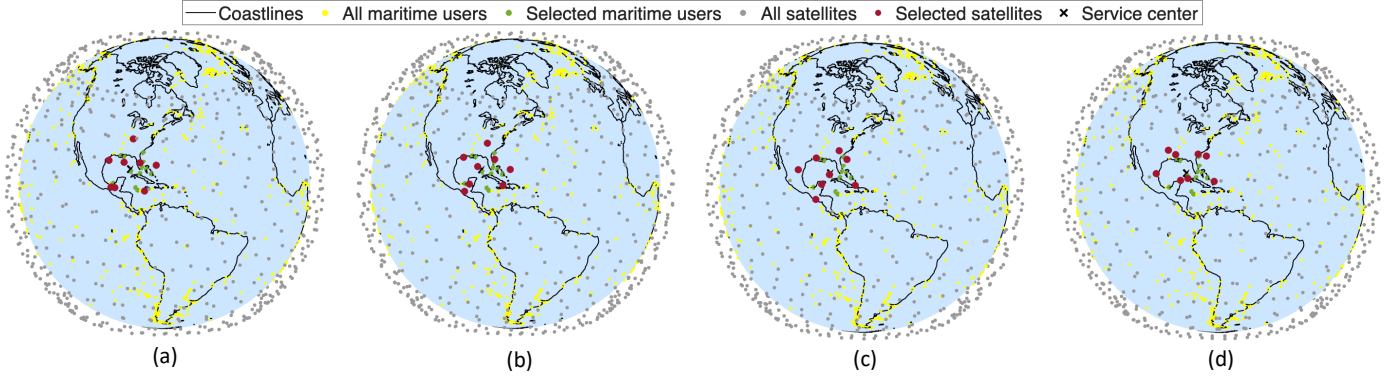


Fig. 3. Frame-wise variation of the serving satellite set $\mathcal{L}^{(k)}$ due to LEO orbital motion. Panels (a)-(d) show the topology snapshots for frames 1-4.

oriented scheduling akin to a strongest-link policy. In Stage (ii), remaining capacity is filled by additionally associating each satellite with the nearest unlinked UTs until U_{\max} is met, thereby prioritizing strong-geometry pairs for extra cooperative links.

- **Correlation-aware:** In Stage (i), we follow the same distance-based policy. In Stage (ii), remaining capacity is filled via a greedy *min-max correlation* criterion: when the ℓ -th satellite considers adding the u -th UT, it computes the maximum normalized channel correlation between u and its currently served set $\mathcal{U}_\ell^{(k)}$, and selects the candidate with the smallest correlation. This discourages serving highly aligned channels simultaneously, improving spatial separability and mitigating IUI.

Given any pre-fixed schedulers from the above rules, cooperative beamformers are optimized under the same QoS constraints and per-satellite radiated power limits as in the proposed joint design, so that performance differences mainly reflect the impact of scheduling decisions. For fairness, all benchmark schemes adopt the same two-segment frame structure and handover-aware metrics as the proposed method: in each frame, a benchmark first determines schedulers and then optimizes beamforming, while the induced inter-frame handover events are evaluated using the segmented-rate and handover-aware power models in Section III.

2) *Non-Cooperative Baselines:* To highlight the role of cooperation, we also consider non-cooperative baselines. The scheduling follows the same three pre-fixed rules as above, with the additional restriction that each UT is served by *exactly one* satellite. Each serving satellite then applies maximum ratio transmission (MRT) toward its scheduled UTs, avoiding inter-satellite coordination and joint beamformer optimization. This isolates a fully non-cooperative mode, at the cost of losing the spatial-DoF and interference-management gains of networked LEO coordination.

B. Simulation Results

1) *Time-Evolution Performance Under Dynamic Topology:* Figure 4(a) illustrates how the serving set $\mathcal{L}^{(k)}$ changes over 6 consecutive frames due to orbital motion (see also Fig. 3

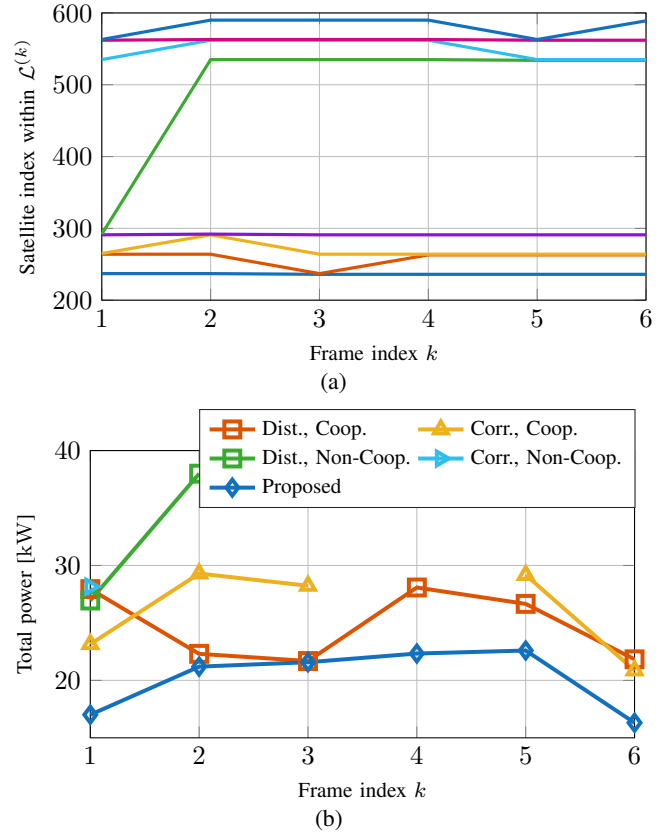


Fig. 4. Time-evolution performance under dynamic topology over 6 consecutive frames. (a) The serving set $\mathcal{L}^{(k)}$ varies across frames due to orbital motion. (b) Network-wide power consumption versus frame index.

for a visualization of the frame-wise serving-set variation), while Fig. 4(b) compares the resulting time-evolution of the network-wide power consumption across different schemes. Importantly, handover introduces an inter-frame coupling: for any frame $k > 1$, both the handover-related cost and the effective (two-segment) rate depend on the scheduling pair between frames $k - 1$ and k , so a short-sighted per-frame design may incur unnecessary switching and hence higher power. As observed in Fig. 4(b), the proposed handover-aware joint cooperative beamforming and user scheduling achieves the lowest power consistently over time, outperforming both the non-cooperative baseline and cooperative baselines with

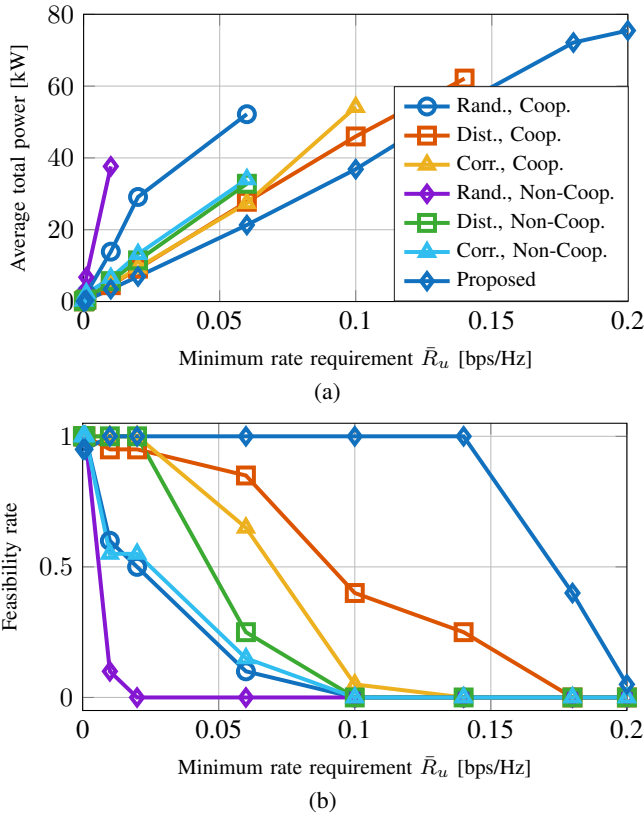


Fig. 5. Average network-wide power consumption and feasibility rate versus the per-UT QoS requirement. (a) Average power consumption computed over feasible trials. (b) Feasibility rate.

pre-fixed scheduling. Moreover, the proposed method remains feasible in all frames in this experiment, whereas several baselines suffer from service interruption in some frames due to infeasibility, which further validates the robustness of the proposed joint design for dynamic LEO topology with frequent handover events.

2) Average Power Consumption Versus QoS Requirement:

Figures 5(a) and (b) report the average network-wide power consumption and the feasibility rate (over 100 Monte-Carlo trials) as functions of the per-UT QoS requirement for all compared schemes. The average power is computed only over the feasible trials. As shown in the figures, the non-cooperative baselines require substantially higher power and become infeasible more frequently than the cooperative designs. An exception is the random-scheduling cooperative baseline, which can also perform poorly since the scheduling stage ignores channel/geometry compatibility and may create an unfavorable interference pattern. Moreover, among the cooperative schemes, Fig. 5(a) shows that the proposed joint cooperative beamforming and user scheduling achieves the lowest average power compared with counterparts using pre-fixed schedulings. These results highlight the value of *multi-LEO cooperation*, which provides additional spatial DoF to better suppress IUI and improve the link budget through network-wide coordination.

3) Average Power Consumption Versus UT Number:

Figures 6(a) and (b) plot the average network-wide power consumption and the feasibility rate, respectively, versus the

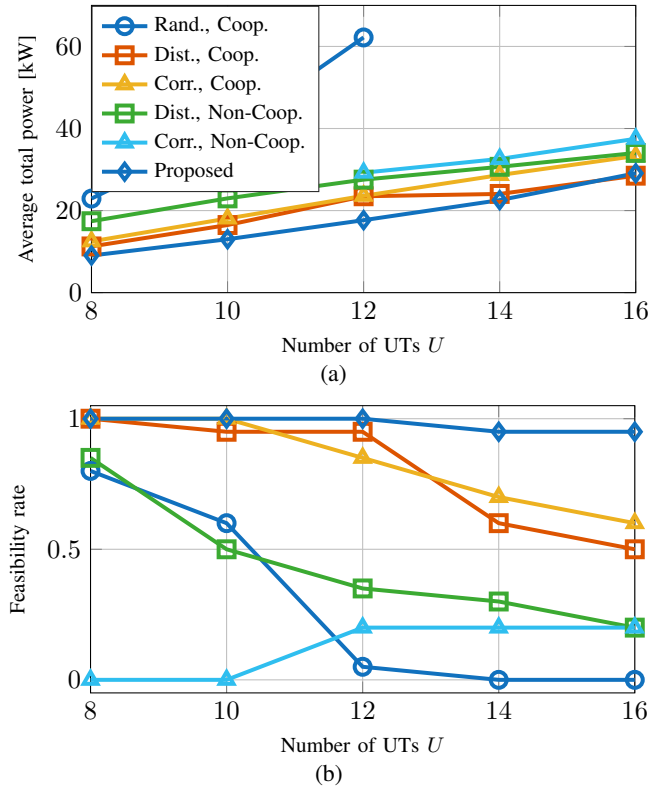
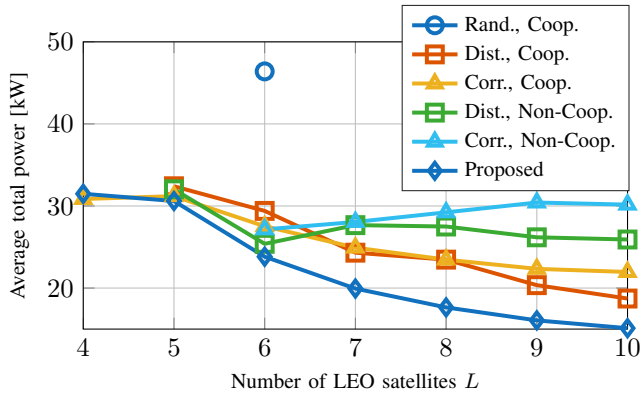


Fig. 6. Average network-wide power consumption and feasibility versus the number of UTs U . (a) Average power computed over feasible trials only. (b) Feasibility rate.

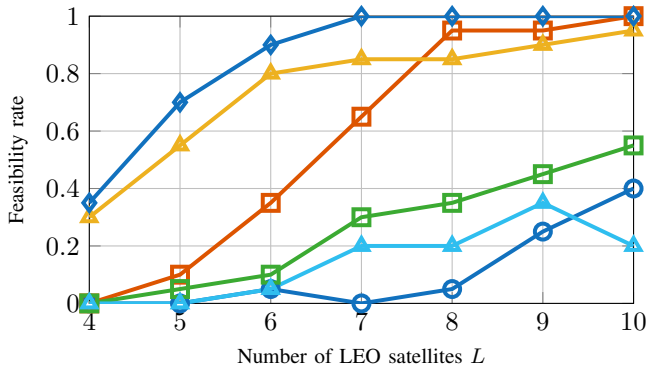
number of UTs U . The average power in Fig. 6(a) is computed only over feasible trials. As expected, increasing U makes the joint scheduling/beamforming problem more constrained (e.g., higher aggregate interference and tighter per-satellite service capacity and power limits), which leads to an increasing power trend and a decreasing feasibility trend for all schemes. Nevertheless, the proposed handover-aware joint cooperative beamforming and user scheduling consistently achieves the lowest power across the whole range of U while maintaining a high feasibility rate in Fig. 6(b), demonstrating that the joint optimization can better reshuffle schedulings and exploit cooperative spatial DoF to mitigate IUI under heavier load. In contrast, a distance-based pre-scheduling baseline may appear to have a comparable power level in some regimes, but its feasibility rate can be substantially lower. Hence, comparing only the averaged power (over feasible trials) may mask its service interruptions.

4) Average Power Consumption Versus LEO Number:

Figures 7(a) and (b) show the average network-wide power consumption (averaged over feasible trials) and the feasibility rate as functions of the number of cooperating LEO satellites in the serving set, denoted by L . When L increases, more satellites participate in joint transmission and additional cooperative DoF becomes available, which improves spatial diversity and interference management. Consequently, the required network-wide power decreases for all cooperative schemes and the feasibility rate improves. Importantly, the proposed handover-aware joint design maintains the best performance and yields the lowest power across different values of L while sustaining a



(a)



(b)

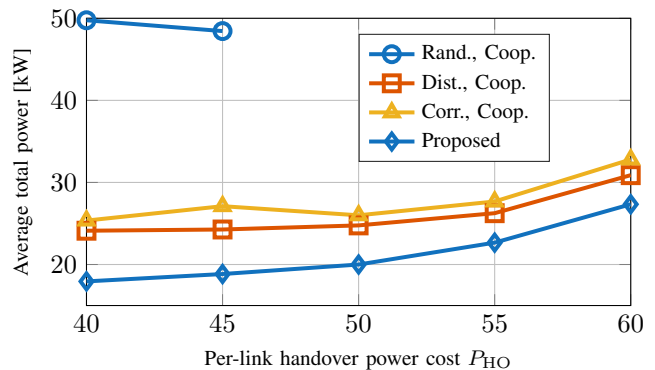
Fig. 7. Average network-wide power consumption and feasibility versus the number of LEO satellites L . (a) Average power computed over feasible trials only. (b) Feasibility rate.

high feasibility rate, confirming that it can effectively leverage the increased cooperation capability without sacrificing robustness.

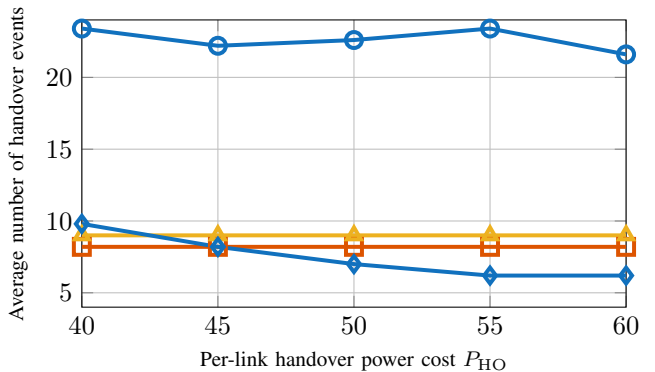
5) *Impact of Handover-Related Power*: Figure 8(a) plots the average network-wide power consumption versus the handover-related power P_{HO} for different cooperative schemes, while Fig. 8(b) reports the corresponding average number of handover events per frame. As P_{HO} increases, scheduling changes become increasingly expensive, and thus the performance depends critically on whether the scheme can jointly balance transmit power and switching cost. As shown in Fig. 8(a), the proposed handover-aware joint cooperative beamforming and user scheduling consistently achieves the lowest power over the entire range of P_{HO} , demonstrating its advantage in adapting to topology variations while meeting the QoS constraints. The random scheduling baseline performs the worst in both power and handover frequency since it does not exploit the geometrical/channel structure and may induce frequent, unnecessary scheduling changes. Finally, Fig. 8(b) shows that the proposed method typically triggers fewer handovers than pre-determined scheduling baselines when P_{HO} is moderate or large, which partly explains the observed power savings.

VI. CONCLUSION

This paper addressed power-efficient downlink operation in networked LEO satellite systems by explicitly accounting for



(a)



(b)

Fig. 8. Impact of handover-related power P_{HO} on network performance. (a) Average network-wide power consumption versus P_{HO} for different cooperative schemes. (b) Average number of handover events versus P_{HO} .

the cost of mobility-induced handovers in the joint design of cooperative beamforming and user scheduling under statistical CSI. A two-segment frame abstraction was introduced to separate handover-related operations from user-plane transmission, which enabled a handover-aware power consumption model capturing both the switching cost of newly activated satellite-UT links and the effective loss of transmission time during handover. Based on the hardening-bound ergodic-rate metric, these ingredients led to a per-frame network-wide power minimization formulation with segmented QoS constraints, per-satellite radiated power budgets, and serving-cardinality limits dictated by the available RFCs.

The resulting problem is intrinsically difficult due to the scheduling-induced sparsity and the nonconvex fractional structure of the statistical-rate constraints. To obtain a tractable solution, we developed an iterative algorithm that integrates a reweighted ℓ_2 surrogate with a penalty-based relaxation and a fractional-programming inner loop, yielding a sequence of convex SOCPs subproblems solvable by standard tools. Simulations driven by systematic time-varying orbital dynamics with frame-wise serving-set evolution and maritime user data quantified the power-handover tradeoff and demonstrated that the proposed handover-aware joint design achieves consistent network-wide power reductions and higher feasibility than non-cooperative baselines and cooperative schemes with pre-fixed scheduling.

Future work may incorporate imperfect ephemeris-aided

compensation and explicit control-plane resource constraints during handover, and develop fully decentralized implementations under limited ISL capacity and latency.

REFERENCES

- [1] I.-R. WP5D. (2022) Future technology trends of terrestrial International Mobile Telecommunications systems towards 2030 and beyond. [Online]. Available: <https://www.itu.int/pub/R-REP-M.2516>
- [2] J. G. Andrews *et al.*, “6G takes shape,” *IEEE BITS the Information Theory Magazine*, vol. 4, no. 1, pp. 2–24, 2024.
- [3] K. Ntontin *et al.*, “A vision, survey, and roadmap toward space communications in the 6G and beyond era,” *Proceedings of the IEEE*, pp. 1–37, 2025.
- [4] 3GPP, “NR; NR and NG-RAN overall description; stage 2,” 3rd Generation Partnership Project, Technical Specification TS 38.300, 2023, release 18.
- [5] —, “Study on New Radio (NR) to support non-terrestrial networks,” 3rd Generation Partnership Project, Technical Report TR 38.811, 2020, release 15.
- [6] M. A. Jamshed *et al.*, “Non-terrestrial networks for 6G: Integrated, intelligent, and ubiquitous connectivity,” *IEEE Communications Standards Magazine*, vol. 9, no. 3, pp. 86–93, 2025.
- [7] L. You *et al.*, “Massive MIMO transmission for LEO satellite communications,” *IEEE Journal on Selected Areas in Communications*, vol. 38, no. 8, pp. 1851–1865, 2020.
- [8] —, “Integrated communications and localization for massive MIMO LEO satellite systems,” *IEEE Transactions on Wireless Communications*, vol. 23, no. 9, pp. 11 061–11 075, 2024.
- [9] Z. Liu *et al.*, “Rate-splitting multiple access for quantized ISAC LEO satellite systems: A max-min fair energy-efficient beam design,” *IEEE Transactions on Wireless Communications*, vol. 23, no. 10, pp. 15 394–15 408, 2024.
- [10] A. U. Chaudhry *et al.*, “Laser intersatellite links in a Starlink constellation: A classification and analysis,” *IEEE Vehicular Technology Magazine*, vol. 16, no. 2, pp. 48–56, 2021.
- [11] Y. Zhang *et al.*, “Enabling scalable distributed beamforming via networked LEO satellites toward 6G,” *IEEE Transactions on Wireless Communications*, vol. 25, pp. 6666–6680, 2026.
- [12] Y. Wang *et al.*, “Statistical CSI-based distributed precoding design for OFDM-cooperative multi-satellite systems,” *IEEE Journal on Selected Areas in Communications*, pp. 1–1, 2026.
- [13] Y. Zhang *et al.*, “Distributed integrated sensing, localization, and communications over LEO satellite constellations,” *IEEE Wireless Communications*, 2026.
- [14] Y. Wang *et al.*, “Multi-satellite multi-stream beamspace massive mimo transmission,” *arXiv preprint arXiv: 2512.21998*, 2025.
- [15] Y. Zhang *et al.*, “Positioning-aided channel estimation for multi-LEO satellite cooperative beamforming,” *IEEE Transactions on Communications*, 2026.
- [16] Z. Xiang *et al.*, “Massive MIMO downlink transmission for multiple LEO satellite communication,” *IEEE Transactions on Communications*, vol. 72, no. 6, pp. 3352–3364, 2024.
- [17] X. Chen *et al.*, “Asynchronous interference mitigation for LEO multi-satellite cooperative systems,” *IEEE Transactions on Wireless Communications*, vol. 23, no. 10, pp. 14 956–14 971, 2024.
- [18] Y. Zhang *et al.*, “Decentralized cooperative beamforming for networked LEO satellites with statistical CSI,” *arXiv preprint arXiv: 2512.18890*, 2025.
- [19] M. Y. Abdelsadek *et al.*, “Distributed massive MIMO for LEO satellite networks,” *IEEE Open Journal of the Communications Society*, vol. 3, pp. 2162–2177, 2022.
- [20] —, “Broadband connectivity for handheld devices via leo satellites: Is distributed massive MIMO the answer?” *IEEE Open Journal of the Communications Society*, vol. 4, pp. 713–726, 2023.
- [21] S. Kim *et al.*, “Cell-free massive non-terrestrial networks,” *IEEE Journal on Selected Areas in Communications*, vol. 43, no. 1, pp. 201–217, 2025.
- [22] X. Zhang *et al.*, “Multi-satellite cooperative networks: Joint hybrid beamforming and user scheduling design,” *IEEE Transactions on Wireless Communications*, vol. 23, no. 7, pp. 7938–7952, 2024.
- [23] E. Juan *et al.*, “Handover solutions for 5G low-Earth orbit satellite networks,” *IEEE Access*, vol. 10, pp. 93 309–93 325, 2022.
- [24] J.-H. Lee *et al.*, “Handover protocol learning for LEO satellite networks: Access delay and collision minimization,” *IEEE Transactions on Wireless Communications*, vol. 23, no. 7, pp. 7624–7637, 2024.
- [25] C. Tong *et al.*, “LEO satellite handover using advantage actor-critic algorithm in giant constellation network,” *IEEE Transactions on Aerospace and Electronic Systems*, vol. 61, no. 5, pp. 11 888–11 903, 2025.
- [26] X. Chen *et al.*, “Handover-aware downlink beamforming design for LEO multibeam satellite communications,” *IEEE Wireless Communications Letters*, vol. 12, no. 6, pp. 947–951, 2023.
- [27] S. Han *et al.*, “Multi-orbit multibeam satellite soft handover strategy based on rate-splitting multiple access,” *IEEE Transactions on Wireless Communications*, vol. 24, no. 8, pp. 6813–6823, 2025.
- [28] T. L. Marzetta *et al.*, *Fundamentals of Massive MIMO*. Cambridge, U.K.: Cambridge University Press, 2016.
- [29] G. Caire, “On the ergodic rate lower bounds with applications to massive MIMO,” *IEEE Transactions on Wireless Communications*, vol. 17, no. 5, pp. 3258–3268, 2018.
- [30] C. A. Balanis, *Antenna Theory: Analysis and Design*. Wiley-Interscience, 2005.
- [31] Y.-Y. He *et al.*, “Physical beam sharing for communications with multiple low Earth orbit satellites,” *IEEE Transactions on Signal Processing*, vol. 72, pp. 2783–2798, 2024.
- [32] J. Moon *et al.*, “Energy-efficient user association in mmWave/THz ultra-dense network via multi-agent deep reinforcement learning,” *IEEE Transactions on Green Communications and Networking*, vol. 7, no. 2, pp. 692–706, 2023.
- [33] K.-X. Li *et al.*, “Channel estimation for LEO satellite massive MIMO OFDM communications,” *IEEE Transactions on Wireless Communications*, vol. 22, no. 11, pp. 7537–7550, 2023.
- [34] G.-Y. Chang *et al.*, “A CSI prediction scheme for satellite-terrestrial networks,” *IEEE Internet of Things Journal*, vol. 10, no. 9, pp. 7774–7785, 2023.
- [35] A. M. Darya *et al.*, “Semi-blind channel estimation for massive mimo LEO satellite communications,” *IEEE Communications Letters*, vol. 29, no. 1, pp. 75–79, 2025.
- [36] T. Yue *et al.*, “Block-based Kalman channel tracking for LEO satellite communication with massive MIMO,” *IEEE Communications Letters*, vol. 27, no. 2, pp. 645–649, 2023.
- [37] M. Ying *et al.*, “Deep learning-based joint channel prediction and multibeam precoding for LEO satellite internet of things,” *IEEE Transactions on Wireless Communications*, vol. 23, no. 10, pp. 13 946–13 960, 2024.
- [38] E. J. Candes *et al.*, “Enhancing sparsity by reweighted l_1 minimization,” *Journal of Fourier analysis and applications*, vol. 14, no. 5, pp. 877–905, 2008.
- [39] G. Kwon *et al.*, “Integrated localization and communication for efficient millimeter wave networks,” *IEEE Journal on Selected Areas in Communications*, vol. 41, no. 12, pp. 3925–3941, 2023.
- [40] G. Zhou *et al.*, “A framework of robust transmission design for IRS-aided MISO communications with imperfect cascaded channels,” *IEEE Transactions on Signal Processing*, vol. 68, pp. 5092–5106, 2020.
- [41] J. Nocedal *et al.*, *Numerical Optimization*. Springer New York, 2006.
- [42] K. Shen *et al.*, “Fractional programming for communication systems—Part I: Power control and beamforming,” *IEEE Transactions on Signal Processing*, vol. 66, no. 10, pp. 2616–2630, 2018.
- [43] —, “Quadratic transform for fractional programming in signal processing and machine learning: A unified approach for solving optimization problems involving ratios,” *IEEE Signal Processing Magazine*, vol. 42, no. 3, pp. 14–34, 2025.
- [44] Y. Zhang *et al.*, “Near-field wideband secure communications: An analog beamfocusing approach,” *IEEE Transactions on Signal Processing*, vol. 72, pp. 2173–2187, 2024.
- [45] H. Al-Hraishawi *et al.*, “Traffic simulator for multibeam satellite communication systems,” in *2020 10th Advanced Satellite Multimedia Systems Conference and the 16th Signal Processing for Space Communications Workshop (ASMS/SPSC)*, 2020, pp. 1–8.
- [46] Q. Wang *et al.*, “Multiple-satellite cooperative information communication and location sensing in LEO satellite constellations,” *IEEE Transactions on Wireless Communications*, vol. 24, no. 4, pp. 3346–3361, 2025.
- [47] T. E. Humphreys *et al.*, “Signal structure of the Starlink Ku-band downlink,” *IEEE Transactions on Aerospace and Electronic Systems*, vol. 59, no. 5, pp. 6016–6030, 2023.